Computed Optical Interferometric Imaging: Methods, Achievements, and Challenges

Fredrick A. South, Yuan-Zhi Liu, P. Scott Carney, and Stephen A. Boppart, *Fellow, IEEE*

(Invited Paper)

Abstract—Three-dimensional high-resolution optical imaging systems are generally restricted by the tradeoff between resolution and depth-of-field as well as imperfections in the imaging system or sample. Computed optical interferometric imaging is able to overcome these longstanding limitations using methods such as interferometric synthetic aperture microscopy (ISAM) and computational adaptive optics (CAO), which manipulate the complex interferometric data. These techniques correct for limited depth-of-field and optical aberrations without the need for additional hardware. This paper aims to outline these computational methods, making them readily available to the research community. Achievements of the techniques will be highlighted, along with past and present challenges in implementing the techniques. Challenges such as phase instability and determination of the appropriate aberration correction have been largely overcome so that imaging of living tissues using ISAM and CAO is now possible. Computed imaging in optics is becoming a mature technology poised to make a significant impact in medicine and biology.

Index Terms—Adaptive optics, biomedical optical imaging, computed imaging, high-resolution imaging, optical coherence tomography, synthetic aperture.

I. INTRODUCTION

IN RECENT decades, optical imaging has become an invaluable tool in medicine and biology. In particular, optical coherence tomography (OCT) has found widespread application in ophthalmology, where it is now the standard-of-care for retinal imaging [1], [2]. OCT is the optical analogue of ultrasound imaging, and uses backscattered light to generate 3-D structural maps of scattering samples of interest [3], [4]. In addition to ophthalmology, OCT has been successfully applied in various other clinical settings as well as non-biological materials imaging [5], [6]. Following a historical trend seen in other modalities such as X-ray imaging, magnetic resonance imaging, and radar, optical imaging is becoming increasingly computational. These computational optical imaging methods have recently become capable of reconstructing *in vivo* data, providing high-resolution aber-ration-free imaging of living biological tissues beyond what was previously achievable by standard OCT imaging alone [7], [8].

The use of computed imaging techniques has been inspired by two inherent limitations ubiquitous in optical imaging—restricted depth-of-field and wavefront aberrations. Limited depth-of-field reduces the usable imaging range, while optical aberrations of both the imaging system and the sample itself limit the achievable resolution and signal-to-noise ratio (SNR).

Various hardware solutions have been proposed to overcome these challenges. In particular, the trade-off between resolution and depth-of-field has been addressed in hardware by focus shifting [9] and multiple beam imaging [10]. Alternatively, a non-Gaussian imaging beam, such as a Bessel beam, can be used to extend the depth-of-field [11], [12]. Inspired by developments in astronomy [13], [14], hardware adaptive optics (HAO) has been used to correct aberrations in microscopy through the use of a wavefront sensor and deformable mirror to sense and negate wavefront distortions [15], [16]. However, HAO systems have not seen widespread use due to their inherent cost and complexity.

It is desirable to achieve high-resolution aberration-free volumetric imaging without the need for additional hardware. Interferometric detection provides access to both the amplitude and the phase of the backscattered light. Access to this phase information provides computational control of the full complex wavefront, enabling refocusing and correction of higher order optical aberrations. Computational depth-of-field solutions include numerical refocusing [17]–[19], depth-encoded synthetic aperture microscopy [20], [21], holoscopy [22], and interferometric synthetic aperture microscopy (ISAM) [23]. Aberration correction can also be performed through manipulation of the spatial frequency data. This has been previously achieved in digital holographic microscopy for imaging of thin samples [24], [25], and recently in thick tissue samples using computational adaptive optics [26], [27].

ISAM is a solution to the inverse problem for optical microscopy that provides depth-independent transverse resolution, overcoming the traditional depth-of-field limitation without the need for additional hardware [23], [28]–[30].

F. A. South, Y.-Z. Liu, and P. S. Carney are with the Beckman Institute for Advanced Science and Technology, and also with the Department of Electrical and Computer Engineering, University of Illinois at Urbana-Champaign, Urbana, IL 61801 USA (e-mail: south1@illinois.edu; yzliu@illinois.edu; carney@illinois.edu).

S. A. Boppart is with the Beckman Institute for Advanced Science and Technology, and also with the Department of Electrical and Computer Engineering, Department of Bioengineering, and Department of Internal Medicine, University of Illinois at Urbana-Champaign, Urbana, IL 61801 USA (e-mail: boppart@illinois.edu).

ISAM reconstruction achieves this through a Fourier domain resampling which provides 3-D defocus correction. ISAM is a point-scanning method, which avoids the cross-talk artifacts inherent in related full-field techniques [19], [22], [31]. It has been shown to be robust with respect to motion through the use of high scanning speeds or motion correction algorithms, and is parallelizable for real-time processing on a graphics processing unit (GPU) [7], [32]. Together, these features have contributed to the successful *in vivo* application of the ISAM technique.

Computational adaptive optics (CAO) extends the ISAM model to include optical aberrations which can be corrected through manipulation of the complex interferometric data [26]. This is achieved by multiplication with a phase-only aberration correction filter which negates the wavefront aberrations. In this way, volumetric aberration-free imaging can be achieved. This flexible processing method can be used to correct for arbitrary aberrations of high order [8], [33], and can be optimized for selected sample regions to overcome spatially varying aberrations [34]. CAO has recently been applied to *in vivo* imaging of the human retina for visualization of the photoreceptor mosaic [8].

This paper will explain both the theory and practical implementation of the ISAM and CAO methods. In addition, the various technical challenges encountered will be addressed along with proposed methods for overcoming these challenges. Key results will be summarized throughout the review, ending with discussion of current and future directions for these computational techniques.

II. INTERFEROMETRIC SYNTHETIC APERTURE MICROSCOPY

This section provides an overview of the ISAM model as well as the necessary steps for implementing the reconstruction. Stability requirements and methods for overcoming phase instability are also discussed. Lastly, the capability of *in vivo* ISAM reconstruction is demonstrated.

A. Theoretical Model

ISAM is performed using low coherence interferometry. In summary, broadband near-infrared light is focused into the sample of interest, and the reflected light is interferometrically detected in the spectral domain. Point scanning in the transverse dimension provides a 3-D complex dataset $S(x, y; k)$ which is a function of transverse position (x, y) and wavenumber k. Under the first Born approximation, the measured signal is given by the convolution of the sample scattering potential $\eta(x, y, z)$ with the system point-spread function (PSF) $h(x, y, z; k)$ as

$$S(x, y; k) = \iiint h(x - x', y - y', z'; k) \eta(x', y', z') \\ \times dx' dy' dz'. \tag{1}$$

The PSF of the system is defined as

$$h(x, y, z; k) = \mu_r k^2 |P(k)|^2 g^2(x, y, z; k), \tag{2}$$

where μ_r is the interferometric power splitting ratio, $|P(k)|^2$ is the power spectral density, and $g^2(x, y, z; k)$ is the product of the identical Gaussian illumination and detection beams. The axial origin of the coordinate system is set as the focal plane $z = 0$ without loss of generality. Using the convolution theorem, Equation (1) can be rewritten in the spatial frequency domain as

$$\tilde{S}(Q_x, Q_y; k) = \int H(Q_x, Q_y, z'; k) \tilde{\eta}(Q_x, Q_y, z') \, dz' \tag{3}$$

where $(\tilde{\ })$ represents the 2-D Fourier transform and Q denotes spatial frequency.

In general, the frequency domain response is depth-dependent. However, using asymptotic approximations for both the near-focus and far-from-focus cases, Equation (3) can be simplified to the forward model

$$\tilde{S}(Q_x, Q_y; k) = H(Q_x, Q_y; k) \approx\!\!\!\!\tilde{\eta}(Q_x, Q_y, Q_z), \tag{4}$$

where $(\approx)$ represents the 3-D Fourier transform and

$$Q_z = -\sqrt{4k^2 - Q_x^2 - Q_y^2}. \tag{5}$$

The system response $H(Q_x, Q_y; k)$ takes slightly different forms for the near- and far-from-focus cases, and in theory it must be inverted to fully recover the scattering potential (a detailed treatment of the system response function can be found in Ref. [30]). However, the system response is generally slowly varying within the pass-band and does not introduce significant image distortions [7], [30], [32]. Therefore, Equation (4) can be inverted through a Fourier domain resampling of the data according to the relationship

$$k = \frac{1}{2}\sqrt{Q_x^2 + Q_y^2 + Q_z^2}. \tag{6}$$

This recovers the unfiltered solution of the scattering potential in the frequency domain

$$\widetilde{\eta}^+(Q_x, Q_y, Q_z) = \tilde{S}(Q_x, Q_y; k)\big|_{k = \frac{1}{2}\sqrt{Q_x^2 + Q_y^2 + Q_z^2}} \tag{7}$$

which can be returned to the spatial domain by the 3-D inverse Fourier transform

$$\eta^+(x, y, z) = F^{-1}\left\{\widetilde{\eta}^+(Q_x, Q_y, Q_z)\right\}. \tag{8}$$

The coordinate resampling step in Equation (7) represents the re-phasing of the 3-D spatial frequency content, and is comparable to Stolt mapping in synthetic aperture radar [35]. In addition, a helpful analogy can be drawn between ISAM and diffraction tomography [30], [36]. The measured spatial frequency vector $\mathbf{Q}$ is given by the difference of the output and input k-vectors $\mathbf{k}_{\text{out}}$ and $\mathbf{k}_{\text{in}}$,

$$\mathbf{Q} = \mathbf{k}_{\text{out}} - \mathbf{k}_{\text{in}}. \tag{9}$$

In the far-from-focus approximation, $\mathbf{k}_{\text{out}} = -\mathbf{k}_{\text{in}}$ and therefore $\mathbf{Q} = -2\mathbf{k}_{\text{in}}$. Considering the entire range of illumination angles within the imaging beam, the measured spatial frequencies trace out a wedge of radius $2k$ on the Ewald sphere [37]. Calculation of the square magnitude of $\mathbf{Q}$ gives the relationship

$$Q_x^2 + Q_y^2 + Q_z^2 = 4k^2, \tag{10}$$

which simplifies immediately to the ISAM coordinate resampling as in Equation (6).

TABLE I
THREE-DIMENSIONAL ISAM PROCESSING STEPS

1. Begin with the dataset $S(x, y; k)$.
2. Calculate the 1-D inverse Fourier transform to retrieve the complex dataset $S(x, y, z)$, keeping only the positive depths $z > 0$.
3. If desired, zero-pad the signal along depth z to improve the subsequent frequency-domain resampling.
4. Circularly shift along depth z to place the focal plane at $z = 0$.
5. Calculate the 3-D Fourier transform to retrieve $\tilde{S}(Q_x, Q_y; k)$.
6. Resample $\tilde{S}(Q_x, Q_y; k)$ along k according to Equation (6) to retrieve the frequency-domain scattering potential $\widetilde{\tilde{\eta}}^+(Q_x, Q_y, Q_z)$.
7. Calculate the 3-D inverse Fourier transform of $\widetilde{\tilde{\eta}}^+(Q_x, Q_y, Q_z)$ to retrieve the reconstructed scattering potential $\eta^+(x, y, z)$.
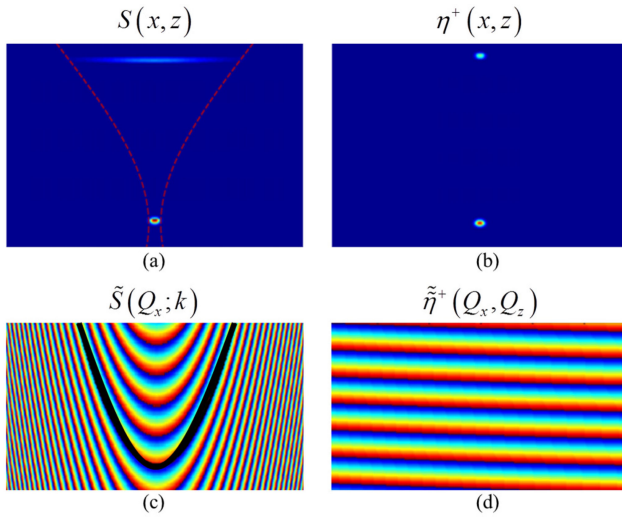

Fig. 1. Simulation of in focus and far-from-focus scattering particles. (a) Cross-section of the standard OCT reconstruction showing strong defocus. (b) ISAM reconstruction showing high-resolution throughout depth. (c) Frequency-domain representation of original dataset. Black line illustrates ISAM resampling curve. (d) Resampled frequency-domain data. Adapted from [26].

B. Implementation

The ISAM imaging system is essentially identical to that used in OCT imaging, achieving resolutions of 1–10 μm and imaging depths of 1–3 mm in tissue. The key difference is that the numerical aperture (NA) may be increased without sacrificing depth-of-field, and further, a higher NA is often used to achieve higher transverse resolution. The NA used in ISAM typically ranges from 0.05 to 0.1 [7], [23]. Recently, ISAM was demonstrated at 0.6 NA for optical coherence microscopy, removing the need for z-stacking [38].

Detailed steps for the implementation of the ISAM reconstruction are listed in Table I. The ISAM simulation for a point-scattering sample shown in Fig. 1 illustrates the data resampling process. The initial curvature of the data in the spatial frequency domain is corrected through appropriate resampling, resulting in a reconstruction with depth-independent resolution. Note that ISAM processing is in addition to any spectral-domain OCT processing steps such as k-linearization, apodization, and dispersion correction.

Alternatively, ISAM can be decomposed into two orthogonal 2-D reconstructions for improved processing speed, which
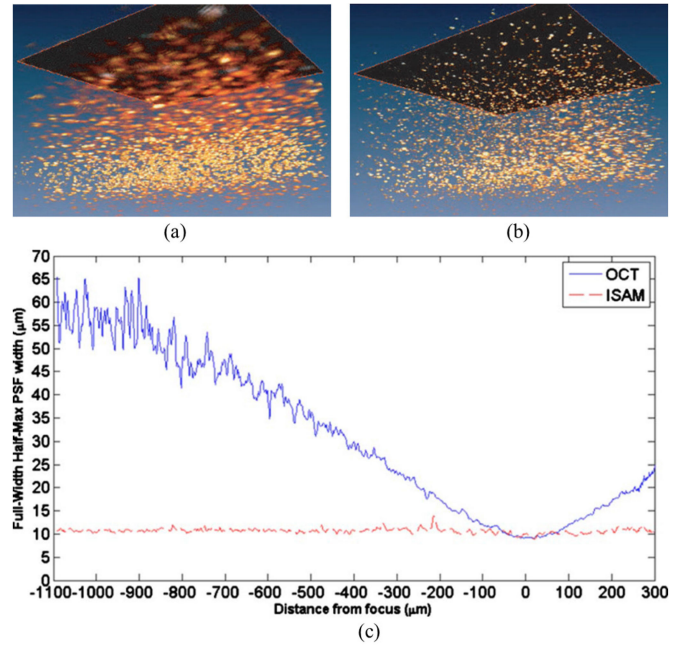

Fig. 2. Comparison of OCT and ISAM reconstructions of TiO$_2$ scattering phantoms imaged with an 800 nm, 0.05 NA OCT system. Transverse dimensions of the rendered volume are 360 μm by 360 μm. (a) 3-D OCT reconstruction. (b) 3-D ISAM reconstruction. (c) Transverse resolution throughout depth for OCT and ISAM experimentally demonstrating that ISAM achieves extended depth-of-field. Adapted from [23] and [39].

enables real-time reconstruction using a GPU [7], [32]. In this scenario, each cross-sectional frame along the fast scanning axis is immediately reconstructed when acquired. Following acquisition of the entire volume, the cross-sectional frames are processed along the slow scanning axis for a complete 3-D reconstruction.

ISAM has been validated in both scattering phantoms and biological tissue. OCT and ISAM reconstructions of a TiO$_2$ scattering phantom are shown in Fig. 2(a) and (b). The limited depth-of-field is clear in the OCT rendering, while ISAM shows high-resolution throughout the volume. A plot of measured transverse resolution over depth is shown in Fig. 2(c). An *en face* plane approximately eight Rayleigh ranges (450 μm) above the focus was selected for comparison. The beam focus was then moved to the plane of interest and an additional OCT reconstruction was generated. The ISAM reconstruction of the out-of-focus plane was shown to match the structure of the in-focus OCT measurement [39].

ISAM also provides an accurate reconstruction of biological tissue structure. This was demonstrated in *ex vivo* human breast tissue where OCT and ISAM reconstructions were compared to the corresponding histology. As a result of high transverse resolution throughout the entire imaging depth, ISAM showed a stronger correspondence to histology [23]. These results illustrate the improved capability of ISAM to perform volumetric high-resolution imaging in biological tissue.

C. Phase Stability

ISAM is a phase-sensitive technique which re-phases optical wavefronts via a coordinate resampling. Like other phase
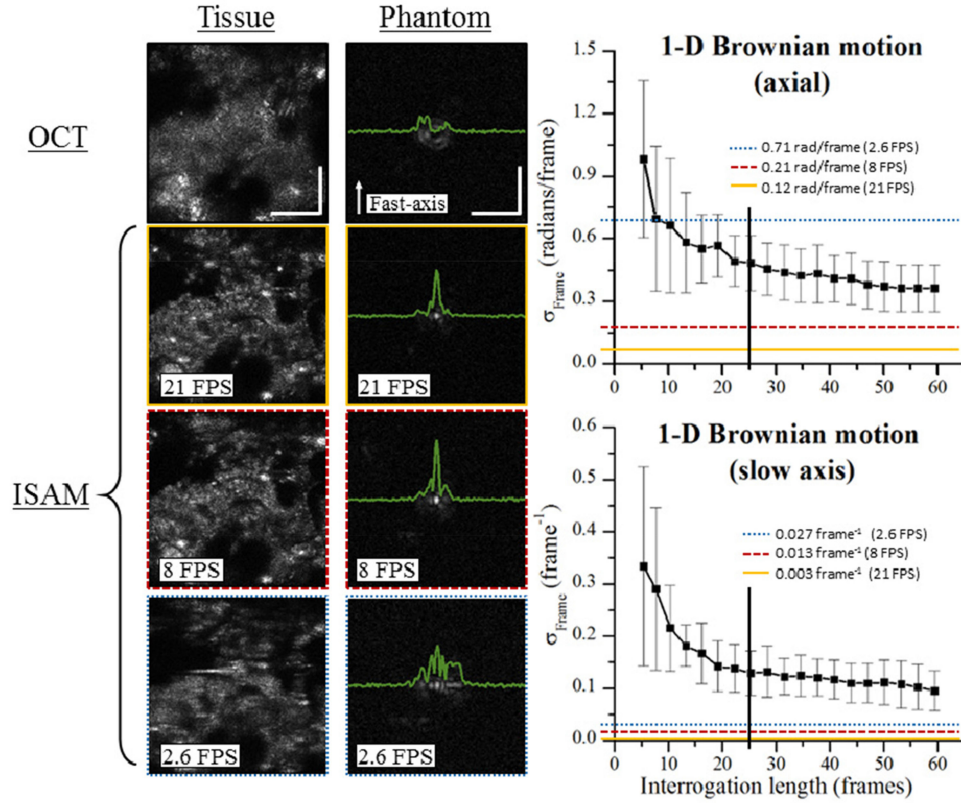
Fig. 3. ISAM reconstructions of *en face* planes and corresponding stability analysis at various imaging speeds for *ex vivo* tissue and a scattering phantom. Images acquired on an 860 nm, 0.6 NA OCT system. Graphs on the right show calculated stability for each imaging speed (horizontal lines) in comparison to previously determined stability requirements (black squares). The approximate interrogation length is indicated by the vertical black line. The axial motion at 2.6 FPS is above the required threshold, and therefore the corresponding ISAM reconstruction fails. Scalebars represent 85 μm for the tissue and 10 μm for the phantom. Reproduced from [41].

sensitive imaging techniques, including CAO, a certain level of phase stability is required for the reconstruction to succeed [40]. To ensure phase stable data, it is necessary to both measure and correct the phase instabilities [41], [42].

Phase instabilities can be caused by motion of the sample or instability of the imaging system itself. Mechanical instability of the reference arm or scanning mirrors can introduce motion artifacts, and sample motion is often unavoidable in living tissues. In either case, it is necessary that the phase be stable over the interrogation time or interrogation length. The interrogation time is the duration for which the scanning Gaussian beam illuminates or "interrogates" a scattering particle. The interrogation time will be greater for particles far-from-focus, as the beam diameter is larger than at the focus. Therefore, phase stability requirements become stricter farther from focus.

Motion can occur along both the axial and transverse directions. The requirements for the axial dimension are defined in terms of the standard deviation of the phase in units of radians per frame. Requirements in the transverse dimension are defined in terms of transverse resolution elements per frame. The effect of phase instability on computational reconstruction is shown in Fig. 3 for both *ex vivo* tissue and scattering phantom data. For high scanning speeds, the phase variation is well below the threshold of approximately 0.3 rad/s. However, at the slowest scanning speed, the axial phase instability is too large to achieve

TABLE II
AXIAL MOTION CORRECTION PROCESSING STEPS

1.	Begin with the complex OCT dataset $S(x, y, z)$.
2.	Calculate the axial phase shift across the slow axis (y) by complex conjugate multiplication of adjacent frames $S(x, y_i, z) \times S^*(x, y_{i+1}, z)$.
3.	Depth-average the resulting complex signal over the depth (z) containing the imaging sample, resulting in a 2-D axial motion map $A(x, y)$.
4.	Set the phase difference to zero for the first frame. Calculate the cumulative sum along the slow axis (y) to convert incremental phase changes to cumulative phase changes.
5.	Smooth the axial phase map using a mean filter along the fast axis (x).
7.	Apply the motion map correction by complex conjugate multiplication at each depth $A^*(x, y) \times S(x, y, z_i)$.

an accurate reconstruction. This demonstrates that motion can be largely mitigated using high scanning speeds.

Both simulation and experiment have demonstrated that computational techniques are most sensitive to phase fluctuations along the axial dimension. The steps for measurement and correction of axial motion are described in Table II. (See Ref. [42] for a detailed discussion of transverse motion correction.) Calculation of an *en face* axial motion phase map $A(x, y)$ is used to negate the axial motion through complex conjugate multiplication with the complex data $S(x, y, z)$. The result is phase stable data to which various computed imaging techniques can be applied. A representative motion map is shown in Fig. 4.
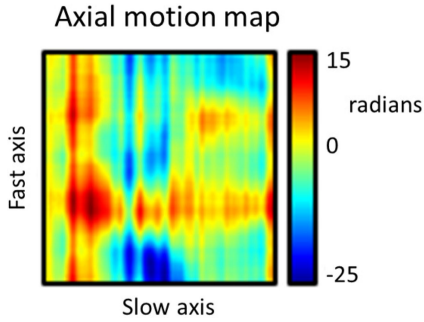
Fig. 4. Axial motion map resulting from the steps outlined in Table II showing smoothed cumulative phase variations. Adapted from [42].
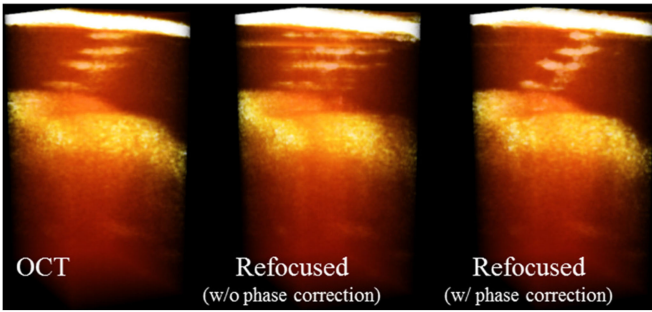

Fig. 5. Image reconstruction of *in vivo* human skin showing the spiral sweat duct structure acquired using a 1300 nm, 0.075 NA OCT system. Prior to phase correction the refocusing fails drastically. Following phase correction the refocused data shows enhanced resolution of the tissue structure. Transverse dimensions of the rendered volume are 250 μm $\times$ 250 μm. Adapted from [42].

Sample motion can be reduced through physically stabilizing the sample using mounting hardware. For skin imaging, this can be accomplished with an objective mount requiring physical contact between the sample arm hardware and the skin [7], [38], [41]. Unfortunately, this type of solution is not feasible for some important imaging applications such as retinal imaging. In these cases motion correction solutions must be applied.

Low SNR does not have the same destructive effect as phase instability. This has been verified in simulation and experiment where ISAM did not fail despite the effective SNR being decreased by as much as 18 dB [40].

D. In Vivo Imaging

By careful consideration of phase stability requirements it is possible to perform *in vivo* imaging [7], [42]. Fig. 5 illustrates the results of computational reconstruction with and without motion correction. The sample was mounted separately from the imaging hardware and was therefore free to move. Without motion correction, the reconstruction clearly fails. After implementing 3-D motion correction, the reconstruction succeeds. These results suggest that the motion correction algorithms are robust enough to enforce phase stability in a variety of living tissues.

A detailed comparison of *in vivo* OCT and ISAM imaging is given in Fig. 6 showing skin images in the fingerprint region of the human index finger. This data was acquired under physical contact with an objective mount at approximately 100 frames/s, which mitigated sample motion. Therefore, no phase stabilization was required. Using the 2-D ISAM processing scheme summarized in Section II-A, the data was processed and displayed in real-time using a GPU.

Anatomical structure was more accurately resolved throughout depth in the ISAM reconstruction. In addition to providing depth-independent resolution, ISAM also provided improvement in other image metrics. ISAM showed improved SNR away from focus when compared to OCT. Because depth-of-field was not a concern, the optical focus was placed deep into tissue, providing increased signal collection at greater depths. This improved both anisotropy [43] and image contrast. The high-quality volumetric visualization of tissue microstructure provided by ISAM could be of key clinical importance for diagnosis of skin disease [44], [45].

III. COMPUTATIONAL ADAPTIVE OPTICS

This section provides an overview of CAO theory as an extension of the ISAM model, including the typical CAO processing steps. Methods of determining the appropriate aberration correction are addressed. The combination of CAO and ISAM is demonstrated in both scattering phantoms and biological tissues.

A. Theory

Significant aberrations exist in many imaging scenarios due to imperfections of the imaging optics or the sample itself. These imperfections distort the phase of the optical wavefront and significantly degrade imaging quality. Examples of commonly encountered aberrations include astigmatism and spherical aberration.

Aberrations may be modeled as a phase-only linear filter which modifies the objective lens pupil function [26], [36]. Within the volume of stationarity $V(x_0, y_0, z_0)$ centered at position (x_0, y_0, z_0), a particular wavefront description is valid. The corresponding aberration phase filter can be written as $H(Q_x, Q_y; k)|_{V(x_0, y_0, z_0)}$. This filter can be applied to the previously derived ISAM model, and Equation (4) can be modified to

$$\tilde{S}_{\mathrm{A}}\left(Q_x, Q_y; k\right)\Big|_{V(x_0, y_0, z_0)} = H_{\mathrm{A}}\left(Q_x, Q_y; k\right)|_{V(x_0, y_0, z_0)}$$
$$\times H\left(Q_x, Q_y; k\right)\widetilde{\eta}\left(Q_x, Q_y, Q_z\right). \quad (11)$$

The aberration effects can be inverted through phase conjugation using the inverse filter

$$H_{\mathrm{AC}}\left(Q_x, Q_y; k\right)|_{V(x_0, y_0, z_0)} = H_{\mathrm{A}}^*\left(Q_x, Q_y; k\right)|_{V(x_0, y_0, z_0)} \quad (12)$$

which results in the aberration-free signal

$$\tilde{S}_{\mathrm{AC}}\left(Q_x, Q_y; k\right)\Big|_{V(x_0, y_0, z_0)} = H_{\mathrm{AC}}\left(Q_x, Q_y; k\right)|_{V(x_0, y_0, z_0)}$$
$$\times \tilde{S}_{\mathrm{A}}\left(Q_x, Q_y; k\right)\Big|_{V(x_0, y_0, z_0)}. \quad (13)$$

If the aberrations can be considered invariant over the transverse field-of-view, the aberration and correction filters can be
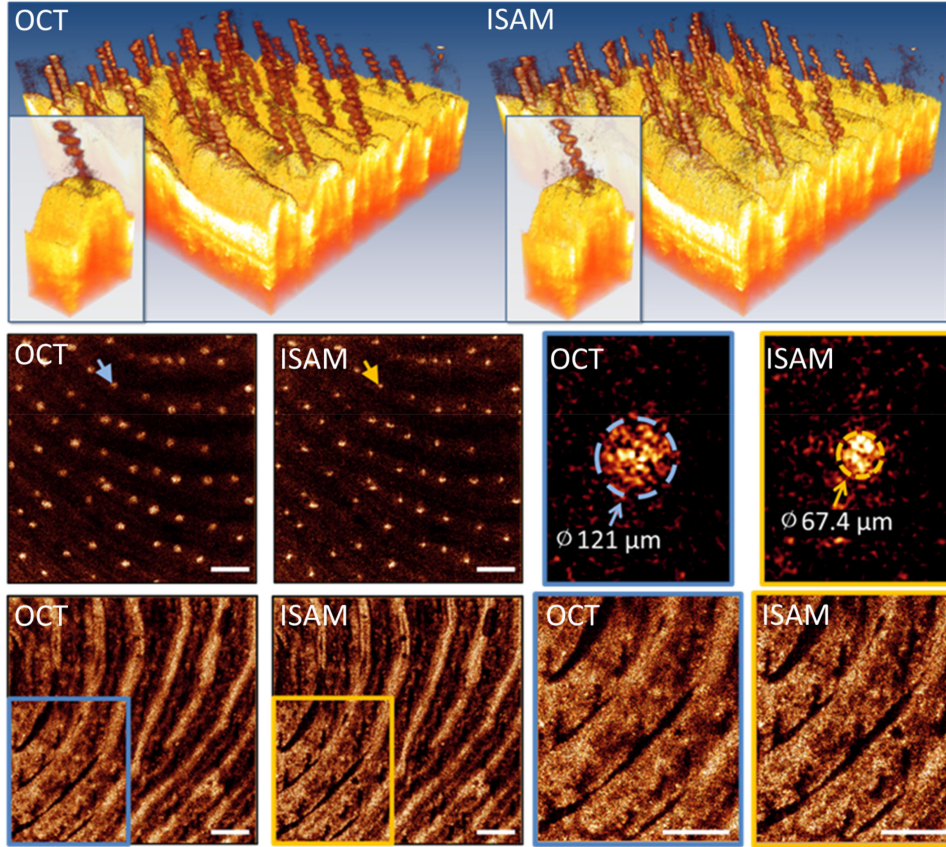
Fig. 6. Visualization of the *in vivo* sub-surface human fingerprint using OCT and ISAM acquired using a 1300 nm, 0.1 NA OCT system. Blue and yellow markers indicate the zoomed regions for OCT and ISAM, respectively. Top row: 3-D rendering of spiral sweat duct structures. Middle row: *En face* plane showing a representative cross section of the sweat ducts. The measured diameter of the ISAM reconstruction is more anatomically correct. Bottom row: *En face* plane of the superficial dermis 780 μm into tissue. Scale bars represent 500 μm. Adapted from [7].

simplified to $H_A(Q_x, Q_y; k)|_{V(z_0)}$ and $H_{AC}(Q_x, Q_y; k)|_{V(z_0)}$, respectively.

B. Implementation

The aberration correction filter $H_{AC}(Q_x, Q_y; k)|_{V(z_0)}$ is related to both the spatial frequency and spectral domains, so it can correct both monochromatic as well as chromatic aberrations [30], [33]. Under the assumption of an achromatic system, the k-dependence of the 3-D aberration correction filter can be simplified to the monochromatic aberration function, $H_{AC}(Q_x, Q_y)|_{V(z_0)}$. The steps for applying CAO processing are summarized in Table III. It is noted that if the aberrations vary considerably within the transverse field-of-view at a given depth, one can divide the image field into sub-regions and implement processing steps 2–5 on each sub-region. The aberration corrected sub-regions can then be recombined to retrieve the composite image for each depth [33]. In some special cases where the dominant artifacts are space-invariant along depth, the same aberration correction filter can be applied to the entire 3-D volume to speed up the computation.

Fig. 7 demonstrates aberration correction by applying CAO. The dataset was measured from a silicone phantom with subresolution TiO_2 microparticles illuminated by a highly astigmatic beam. *En face* planes following standard OCT processing show

TABLE III
CAO PROCESSING STEPS

1.	Begin with the complex OCT or ISAM dataset $S_A(x, y, z)$.
2.	Calculate the 2-D Fourier transform of *en face* image fields at each depth z_i, $\tilde{S}_A(Q_x, Q_y, z_i)$.
3.	Calculate the aberration correction filter $H_{AC}(Q_x, Q_y)|_{z_i}$ for the image field.
4.	Apply the aberration correction in the Fourier plane by complex multiplication at each depth $\tilde{S}_{AC}(Q_x, Q_y, z_i) = H_{AC}(Q_x, Q_y)|_{z_i} \times \tilde{S}_A(Q_x, Q_y, z_i)$.
5.	Calculate the 2-D inverse Fourier transform of $\tilde{S}_{AC}(Q_x, Q_y, z_i)$ to retrieve the aberration-free image field, $S_{AC}(x, y, z_i)$.
6.	Stack the *en face* image fields along the depth to obtain the aberration-free volume $S_{AC}(x, y, z)$.

the presence of two orthogonal line foci associated with astigmatism, as well as the plane of least confusion located halfway in between. After correcting the astigmatism, the plane of least confusion was restored as the focal plane and the line foci showed a Gaussian-like PSF. ISAM was then applied, reconstructing the entire volume with high-resolution. Imaging with the astigmatic beam also gave improved SNR far-from-focus as a result of the dual line foci. This suggests that imaging with an aberrated beam may actually be beneficial when the PSF can be computationally corrected.

Many biological samples have been successfully imaged using CAO such as *ex vivo* human breast tissue, *in vitro* 3-D cell
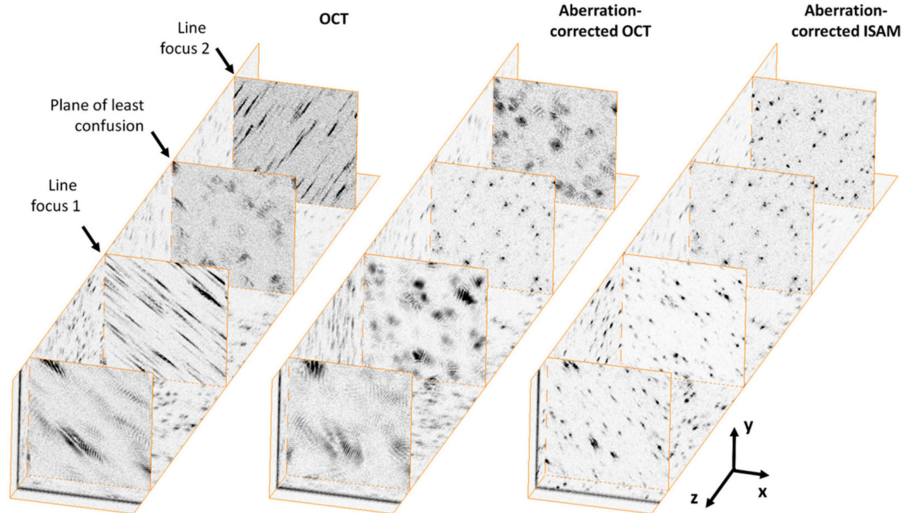
Fig. 7. Demonstration of aberration correction in a scattering phantom using CAO. Images acquired on a 1300 nm, 0.1 NA OCT system. Select *en face* planes have been rendered to highlight the strong astigmatism. CAO restores the focal plane while ISAM improves the depth-of-field. Transverse dimensions of the rendered volume are 256 μm $\times$ 256 μm. Reproduced from [26].
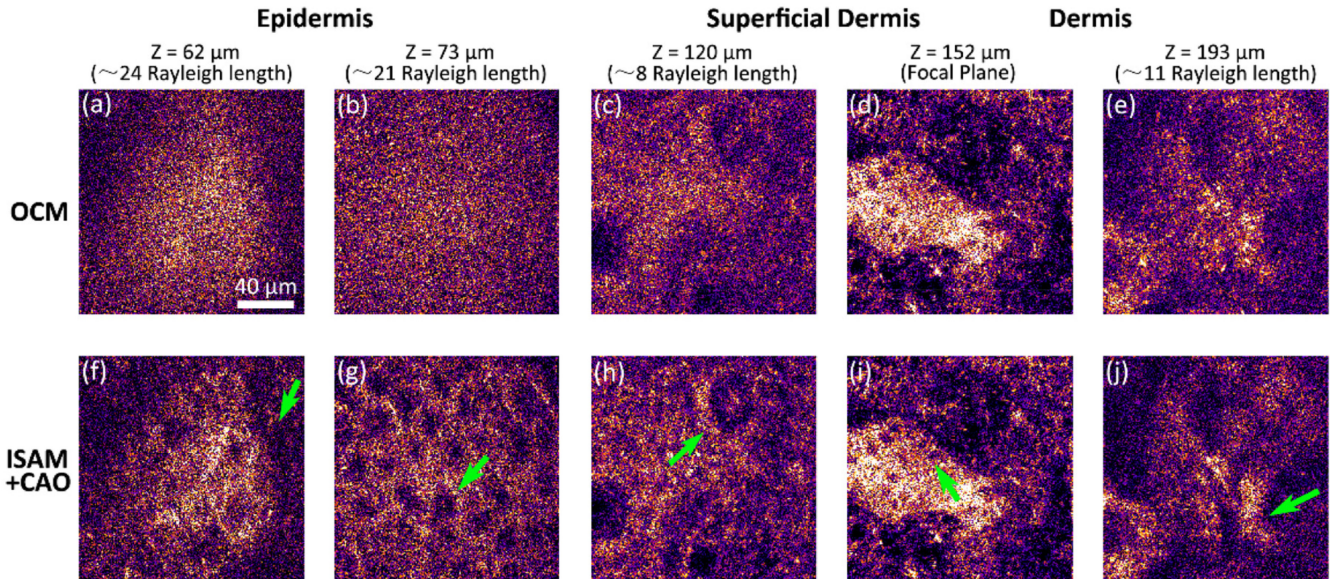

Fig. 8. High-resolution imaging of *in vivo* human skin acquired using an 860 nm, 0.6 NA OCM system. Arrows indicate (a), (f) boundary of the stratum corneum and epidermis, (b), (g) granular cell nuclei, (c), (h) dermal papillae, (d), (i) basal cells, and (e), (j) connective tissue. Scale bar indicates 40 μm and applies to all images. Reproduced from [38].

cultures, and various *ex vivo* animal tissues. As with ISAM, CAO can also be applied to *in vivo* imaging when stability concerns are considered. Fig. 8 demonstrates this capability for 3-D *in vivo* imaging of human skin. Together, the ISAM and CAO methods complement one another to provide 3-D high-resolution images of biological tissue without the need for depth scanning or additional imaging hardware [26], [33], [38].

C. Determining the Correction Filter

Because the optical aberrations of a particular imaging system are generally unknown, it can be a significant challenge to determine the appropriate correction filter. One solution is similar to sensor-less HAO techniques [46]. In sensor-less

HAO, a sequence of aberration corrections beginning with an initial guess is applied using a deformable mirror. Image metrics are then used to assess the subsequent change of the signal or image quality. Instead of physically altering the wavefront, CAO applies a sequence of computational aberration correction filters which are digitally applied to the complex image. The correction filter $H_{\mathrm{AC}}(Q_x, Q_y)|_z$ can be expressed as a modal term as in Zernike polynomial decomposition, or as a zonal-based wavefront. Several image metrics such as peak intensity, spatial frequency content, and image sharpness have been proposed and demonstrated for use in coherent imaging [26], [38], [47].

A technique termed subaperture correlation has also been proposed to digitally correct the aberrations in OCT data [27].
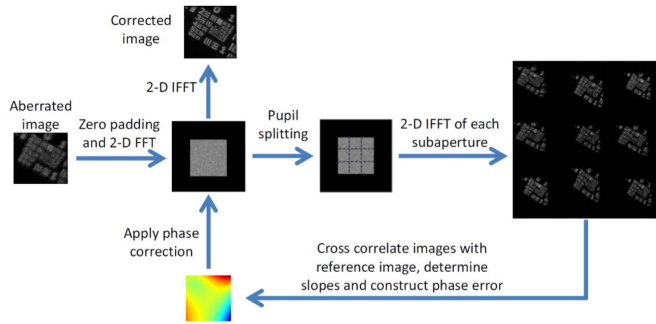
Fig. 9. Illustration of the subaperture method for estimation of the aberration correction filter. Subapertures in the spatial-frequency domain are compared to the central reference subaperture to determine the slope of the wavefront. Reproduced from [27].

Fig. 10. Example wavefront correction for the human eye calculated using the subaperture and guide-star methods. Adapted from [8].

While CAO mimics the behavior of a deformable mirror, the subaperture technique simulates the operation of the Shack-Harman wavefront sensor by dividing the Fourier plane into several subapertures. The wavefront slopes of each subaperture are calculated from the cross-correlation of the reconstructed subaperture images to the center subaperture reference image, as illustrated in Fig. 9. This method has shown image improvement for scattering samples that have a uniform Fourier spectrum, although only low-order aberrations can be corrected.

If the sample contains point-like structures, the so-called "guide-star" method can be used in CAO to correct not only the high-order monochromatic but also the chromatic aberrations [33]. A spatial window is used to capture the entire aberrated PSF of the guide-star, and a sub-resolution window is used to crop the guide-star to the desired target PSF. By isolating the signal from a guide-star, the aberrations can be sensed from the phase difference of the measured and desired wavefront in the Fourier domain. The aberration correction filter can then be digitally conjugated in the Fourier domain and applied to the whole image or 3-D volume of stationarity containing the guide-star. Finally, after the inverse Fourier transform, the aberration-free data can be achieved.

IV. CURRENT RESEARCH

This section discusses current research directions in computed optical interferometric imaging. Efforts are focused on *in vivo* imaging of the human retina, which is currently the most widespread application of OCT and adaptive optics. Imaging of the photoreceptors aids the diagnosis and understanding of diseases such as macular degeneration [48], [49]. Although it is possible to image the photoreceptors without adaptive optics provided the subject's eye has very low aberrations [50], [51], in general this is not the case [52]. As the NA of the imaging beam is increased, aberrations play an increased role and distort the PSF [53], [54]. Because of this, HAO solutions have been used to achieve diffraction-limited imaging of the retina [16]. However, the cost and complexity of HAO has restricted its clinical application. A computational alternative, therefore, is highly desirable.

The eye exhibits frequent and unavoidable motion [55]. This motion poses a significant challenge for computational
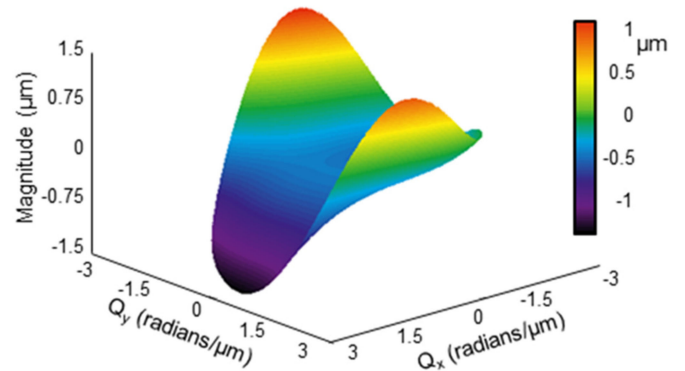
techniques and must be carefully considered. Unlike the skin, direct physical contact of the imaging hardware with the eye is not clinically feasible. Therefore, high scanning speeds and motion correction techniques must be implemented. Transverse motion correction can be avoided by imaging at cross-sectional frame rates greater than 1.5 kHz [56].

The first CAO images of the living human retina were recently reported using an *en face* OCT imaging system [8]. The use of *en face* OCT allowed for a higher effective frame rate in comparison to typical spectral-domain methods. The system operated at 4000 *en face* lines per second, which for stability purposes is equivalent to a spectral-domain OCT system operating at a frame rate of 4 kHz. Even at this high imaging speed, axial motion correction was required due to phase instabilities from the acoustic optic modulators and sample motion. The axial motion correction algorithm outlined in Section II-C was used, slightly modified to work with *en face* data.

The subaperture and guide-star methods discussed in Section III-C were implemented sequentially to determine the appropriate aberration correction filter for imaging the photoreceptor layer. The resulting aberration correction is shown in Fig. 10. The subaperture method was used to determine a bulk correction. The individual photoreceptors served as natural guide-stars to fine-tune the correction, modifying the Zernike polynomial terms of the bulk correction by up to 40%. The resulting photoreceptor mosaic is shown in Fig. 11. The CAO result clearly resolves the individual photoreceptors, gleaning valuable biological information from previously unintelligible data.

Visualization of other retinal layers also benefits from improved resolution. The health of the retinal nerve fiber layer (RNFL) is an important marker for diseases such as glaucoma [57], [58] and multiple sclerosis [59], [60]. These fibers are densely packed and difficult to resolve without aberration correction. CAO imaging of retinal fiber structure is shown in Fig. 12, acquired using the same *en face* imaging system. The aberration correction was manually adjusted to maximize the anisotropy image metric [43]. The previously hidden structure was clearly resolved.

Because HAO physically modifies the optical wavefront, the signal collected from the retina is greatly increased. However, CAO is a post-processing technique which can only redistribute
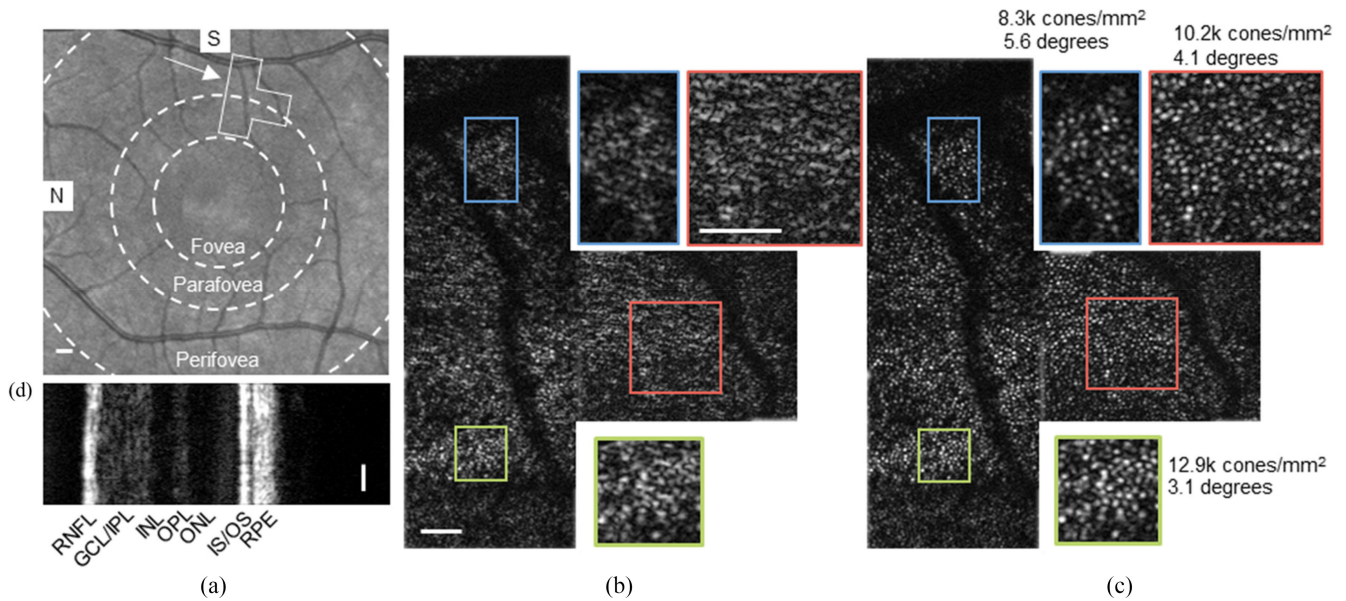
Fig. 11.   Aberration correction in the living human retina using CAO. (a) Scanning laser ophthalmoscope image of the retinal surface. N: nasal, S: superior. OCT images taken in the boxed region. (b) Uncorrected *en face* OCT data shows no recognizable features. (c) Aberration corrected data showing individual photoreceptors. (d) Simultaneously acquired cross-sectional OCT data showing the various retinal layers. The *en face* photoreceptor mosaic was acquired at the IS/OS junction. RNFL: retinal nerve fiber layer, GCL/IPL: ganglion cell layer/inner plexiform layer, INL: inner nuclear layer, OPL: outer plexiform layer, ONL: outer nuclear layer, IS/OS: inner segment/outer segment, RPE: retinal pigment epithelium. Colored boxes correspond to the matching zoomed regions. Scale bar represents 1° in (a) and 0.25° in (b)–(d). Reproduced from [8].
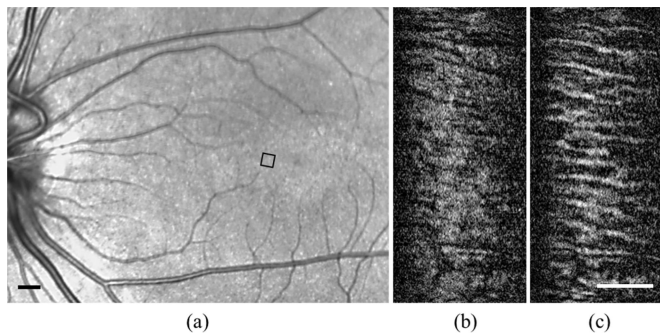

Fig. 12.   CAO of retinal fiber structure. (a) Scanning laser ophthalmoscope image of the retinal surface. The boxed region indicates the approximate OCT imaging location. (b) Uncorrected *en face* OCT data. (c) Data corrected using CAO showing improved resolution of the fiber structure. Scale bar represents approximately 2° in (a) and 0.2° in (b) and (c). Data previously unpublished.

the collected energy. Therefore, in subjects with severe eye disease where there is insufficient signal to generate an initial image, a purely computational solution may not be sufficient. In this case CAO could be supplemented with a low-order hardware correction to provide the necessary signal strength.

V. CONCLUSION

Together, ISAM and CAO are complementary computational methods which achieve high-resolution volumetric optical imaging in living tissue, overcoming both limited depth-of-field and optical aberrations. Moving forward, a primary goal as well as a key challenge will be the translation of these computed imaging techniques to the clinical setting. Computational techniques were previously restricted by phase stability requirements. Recently, however, the challenge of phase stabilization has been largely overcome through motion correction techniques. Implementation of these techniques, however, may vary across clinical imaging scenarios and existing clinical systems may or may not be suitable for phase-sensitive imaging. Aberration correction encounters the additional challenge of determining the appropriate correction filter. Several methods have been proposed, yet it remains to be determined which method will prove most useful for real-time applications.

As with any medical tool, the capability of the technology to improve the performance of clinical tasks must be determined. Since many features in the eye cannot be seen using the current standard-of-care optical imaging technologies, the impact of computational correction is expected to be significant. Application to other clinical areas such as dermatology and oncology may also benefit from the improved image quality. Future studies will involve the imaging of disease in collaboration with medical specialists to assess the true clinical impact of the computational techniques.

In summary, recent research results have demonstrated that computed optical interferometric imaging has matured to supplement and, in some applications, potentially even replace traditional optical tomography in medicine and biology.

S. G. Adie, and N. D. Shemonski. The human subjects research was performed under protocols approved by the Institutional Review Board at the University of Illinois at Urbana-Champaign. S. A. Boppart and P. S. Carney are cofounders of Diagnostic Photonics, Inc., which is licensing intellectual property from the University of Illinois at Urbana-Champaign related to ISAM. S. A. Boppart also received royalties from MIT related to patents related to OCT. Additional information can be found at http://biophotonics.illinois.edu.

REFERENCES

[1] D. Huang *et al.*, "Optical coherence tomography," *Science*, vol. 254, pp. 1178–1181, 1991.

[2] W. Drexler and J. G. Fujimoto, "State-of-the-art retinal optical coherence tomography," *Prog. Retinal Eye Res.*, vol. 27, pp. 45–88, 2008.

[3] J. M. Schmitt, "Optical coherence tomography (OCT): A review," *IEEE J. Sel. Topics Quantum Electron.*, vol. 5, pp. 1205–1215, 1999.

[4] P. H. Tomlins and R. K. Wang, "Theory, developments and applications of optical coherence tomography," *J. Phys. D, Appl. Phys.*, vol. 38, pp. 2519–2539, 2005.

[5] A. M. Zysk, F. T. Nguyen, A. L. Oldenburg, D. L. Marks, and S. A. Boppart, "Optical coherence tomography: A review of clinical development from bench to bedside," *J. Biomed. Opt.*, vol. 12, pp. 051403-1–051403-21, 2007.

[6] D. Stifter, "Beyond biomedicine: A review of alternative applications and developments for optical coherence tomography," *Appl. Phys. B*, vol. 88, pp. 337–357, 2007.

[7] A. Ahmad *et al.*, "Real-time *in vivo* computed optical interferometric tomography," *Nature Photon.*, vol. 7, pp. 445–449, 2013.

[8] N. D. Shemonski *et al.*, "Computational high-resolution optical imaging of the living human retina," *Nature Photon.*, vol. 9, pp. 440–443, 2015.

[9] K.-S. Lee *et al.*, "Three-dimensional imaging of normal skin and non-melanoma skin cancer with cellular resolution using Gabor domain optical coherence microscopy," *J. Biomed. Opt.*, vol. 17, pp. 126006-1–126006-8, 2012.

[10] A. S. Beau *et al.*, "*In vivo* endoscopic multi-beam optical coherence tomography," *Phys. Med. Biol.*, vol. 55, pp. 615–622, 2010.

[11] Z. H. Ding, H. W. Ren, Y. H. Zhao, J. S. Nelson, and Z. P. Chen, "High-resolution optical coherence tomography over a large depth range with an axicon lens," *Opt. Lett.*, vol. 27, pp. 243–245, 2002.

[12] C. Blatter *et al.*, "*In situ* structural and microangiographic assessment of human skin lesions with high-speed OCT," *Biomed. Opt. Exp.*, vol. 3, pp. 2636–2646, 2012.

[13] J. M. Beckers, "Adaptive optics for astronomy: Principles, performance, and applications," *Annu. Rev. Astron. Astrophys.*, vol. 31, pp. 13–62, 1993.

[14] R. Davies and M. Kasper, "Adaptive optics for astronomy," *Annu. Rev. Astron. Astrophys.*, vol. 50, pp. 305–351, 2012.

[15] J. Liang, D. R. Williams, and D. T. Miller, "Supernormal vision and high-resolution retinal imaging through adaptive optics," *J. Opt. Soc. Amer. A*, vol. 14, pp. 2884–2892, 1997.

[16] Y. Zhang *et al.*, "High-speed volumetric imaging of cone photoreceptors with adaptive optics spectral-domain optical coherence tomography," *Opt. Exp.*, vol. 14, pp. 4380–4394, 2006.

[17] Y. Yasuno *et al.*, "Non-iterative numerical method for laterally superresolving Fourier domain optical coherence tomography," *Opt. Exp.*, vol. 14, pp. 1006–1020, 2006.

[18] L. Yu *et al.*, "Improved lateral resolution in optical coherence tomography by digital focusing using two-dimensional numerical diffraction method," *Opt. Exp.*, vol. 15, pp. 7634–7641, 2007.

[19] A. Kumar, W. Drexler, and R. A. Leitgeb, "Numerical focusing methods for full field OCT: A comparison based on a common signal model," *Opt. Exp.*, vol. 22, pp. 16061–16078, 2014.

[20] J. Mo, M. De Groot, and J. F. De Boer, "Focus-extension by depth-encoded synthetic aperture in optical coherence tomography," *Opt. Exp.*, vol. 21, pp. 10048–10061, 2013.

[21] J. Mo, M. De Groot, and J. F. De Boer, "Depth-encoded synthetic aperture optical coherence tomography of biological tissues with extended focal depth," *Opt. Exp.*, vol. 23, pp. 4935–4945, 2015.

[22] D. Hillmann, G. Franke, C. Lührs, P. Koch, and G. Hüttmann, "Efficient holoscopy image reconstruction," *Opt. Exp.*, vol. 20, pp. 21247–21263, 2012.

[23] T. S. Ralston, D. L. Marks, P. S. Carney, and S. A. Boppart, "Interferometric synthetic aperture microscopy," *Nature Phys.*, vol. 3, pp. 129–134, 2007.

[24] T. Colomb *et al.*, "Numerical parametric lens for shifting, magnification, and complete aberration compensation in digital holographic microscopy," *J. Opt. Soc. Amer. A*, vol. 23, pp. 3177–3190, 2006.

[25] L. Miccio *et al.*, "Direct full compensation of the aberrations in quantitative phase microscopy of thin objects by a single digital hologram," *Appl. Phys. Lett.*, vol. 90, p. 041104, 2007.

[26] S. G. Adie, B. W. Graf, A. Ahmad, P. S. Carney, and S. A. Boppart, "Computational adaptive optics for broadband optical interferometric tomography of biological tissue," *Proc. Nat. Acad. Sci. USA*, vol. 109, pp. 7175–7180, 2012.

[27] A. Kumar, W. Drexler, and R. A. Leitgeb, "Subaperture correlation based digital adaptive optics for full field optical coherence tomography," *Opt. Exp*, vol. 21, pp. 10850–10866, 2013.

[28] T. S. Ralston, D. L. Marks, P. S. Carney, and S. A. Boppart, "Inverse scattering for optical coherence tomography," *J. Opt. Soc. Amer. A*, vol. 23, pp. 1027–1037, 2006.

[29] T. S. Ralston, D. L. Marks, S. A. Boppart, and P. S. Carney, "Inverse scattering for high-resolution interferometric microscopy," *Opt. Lett.*, vol. 31, pp. 3585–3587, 2006.

[30] B. J. Davis *et al.*, "Nonparaxial vector-field modeling of optical coherence tomography and interferometric synthetic aperture microscopy," *J. Opt. Soc. Amer. A*, vol. 24, pp. 2527–2542, 2007.

[31] D. L. Marks, T. S. Ralston, S. A. Boppart, and P. S. Carney, "Inverse scattering for frequency-scanned full-field optical coherence tomography," *J. Opt. Soc. Amer. A*, vol. 24, pp. 1034–1041, 2007.

[32] T. S. Ralston, D. L. Marks, P. S. Carney, and S. A. Boppart, "Real-time interferometric synthetic aperture microscopy," *Opt. Exp.*, vol. 16, pp. 2555–2569, 2008.

[33] S. G. Adie *et al.*, "Guide-star-based computational adaptive optics for broadband interferometric tomography," *Appl. Phys. Lett.*, vol. 101, p. 221117, 2012.

[34] A. Kumar *et al.*, "Anisotropic aberration correction using region of interest based digital adaptive optics in Fourier domain OCT," *Biomed. Opt. Exp.*, vol. 6, pp. 1124–1134, 2015.

[35] B. J. Davis, D. L. Marks, T. S. Ralston, P. S. Carney, and S. A. Boppart, "Interferometric synthetic aperture microscopy: computed imaging for scanned coherent microscopy," *Sensors*, vol. 8, pp. 3903–3931, 2008.

[36] S. G. Adie, N. D. Shemonski, T. S. Ralston, P. S. Carney, and S. A. Boppart, "Interferometric synthetic aperture microscopy (ISAM)," in *Optical Coherence Tomography: Technology and Applications*, W. Drexler and J. G. Fujimoto, Eds., 2nd ed. New York, NY, USA: Springer-Verlag, 2015.

[37] M. Born and E. Wolf, *Principles of Optics: Electromagnetic Theory of Propagation, Interference and Diffraction of Light*, 7th ed. Cambridge, U.K.: Cambridge Univ. Press, 1999.

[38] Y.-Z. Liu *et al.*, "Computed optical interferometric tomography for high-speed volumetric cellular imaging," *Biomed. Opt. Exp.*, vol. 5, pp. 2988–3000, 2014.

[39] T. S. Ralston, S. G. Adie, D. L. Marks, S. A. Boppart, and P. S. Carney, "Cross-validation of interferometric synthetic aperture microscopy and optical coherence tomography," *Opt. Lett.*, vol. 35, pp. 1683–1685, 2010.

[40] N. D. Shemonski *et al.*, "Stability in computed optical interferometric tomography (Part I): Stability requirements," *Opt. Exp.*, vol. 22, pp. 19183–19197, 2014.

[41] N. D. Shemonski *et al.*, "Stability in computed optical interferometric tomography (Part II): *In vivo* stability assessment," *Opt. Exp.*, vol. 22, pp. 19314–19326, 2014.

[42] N. D. Shemonski *et al.*, "Three-dimensional motion correction using speckle and phase for *in vivo* computed optical interferometric tomography," *Biomed. Opt. Exp.*, vol. 5, pp. 4131–4143, 2014.

[43] S. Gabarda and G. Cristóbal, "Blind image quality assessment through anisotropy," *J. Opt. Soc. Amer. A*, vol. 24, pp. B42–B51, 2007.

[44] J. Welzel, "Optical coherence tomography in dermatology: A review," *Skin Res. Technol.*, vol. 7, pp. 1–9, 2001.

[45] T. Gambichler *et al.*, "Applications of optical coherence tomography in dermatology," *J. Dermatol. Sci.*, vol. 40, pp. 85–94, 2005.

[46] H. Hofer, N. Sredar, H. Queener, C. H. Li, and J. Porter, "Wavefront sensorless adaptive optics ophthalmoscopy in the human eye," *Opt. Exp.*, vol. 19, pp. 14160–14171, 2011.

[47] J. R. Fienup and J. J. Miller, "Aberration correction by maximizing generalized sharpness metrics," *J. Opt. Soc. Amer. A*, vol. 20, pp. 609–620, 2003.

[48] J. L. Duncan *et al.*, "High-resolution imaging with adaptive optics in patients with inherited retinal degeneration," *Invest. Ophthalmol. Vis. Sci.*, vol. 48, pp. 3283–3291, 2007.

[49] S. Zayit-Soudry, J. L. Duncan, R. Syed, M. Menghini, and A. J. Roorda, "Cone structure imaged with adaptive optics scanning laser ophthalmoscopy in eyes with nonneovascular age-related macular degeneration," *Invest. Ophthalmol. Vis. Sci.*, vol. 54, pp. 7498–7509, 2013.

[50] D. T. Miller, D. R. Williams, G. M. Morris, and J. Liang, "Images of cone photoreceptors in the living human eye," *Vis. Res.*, vol. 36, pp. 1067–1079, 1996.

[51] M. Pircher, B. Baumann, E. Götzinger, and C. K. Hitzenberger, "Retinal cone mosaic imaged with transverse scanning optical coherence tomography," *Opt. Lett.*, vol. 31, pp. 1821–1823, 2006.

[52] L. N. Thibos, X. Hong, A. Bradley, and X. Cheng, "Statistical variation of aberration structure and image quality in a normal population of healthy eyes," *J. Opt. Soc. Amer. A*, vol. 19, pp. 2329–2348, 2002.

[53] J. Liang and D. R. Williams, "Aberrations and retinal image quality of the normal human eye," *J. Opt. Soc. Amer. A*, vol. 14, pp. 2873–2883, 1997.

[54] D. R. Williams, "Imaging single cells in the living retina," *Vis. Res.*, vol. 51, pp. 1379–1396, 2011.

[55] S. Martinez-Conde, S. L. Macknik, and D. H. Hubel, "The role of fixational eye movements in visual perception," *Nature Rev. Neurosci.*, vol. 5, pp. 229–240, 2004.

[56] N. D. Shemonski *et al.*, "A computational approach to high-resolution imaging of the living human retina without hardware adaptive optics," *Proc. SPIE, Ophthalmic Technol. XXV*, vol. 9307, pp. 930710–1–930710-7, 2015.

[57] O. P. Kocaoglu *et al.*, "Imaging retinal nerve fiber bundles using optical coherence tomography with adaptive optics," *Vis. Res.*, vol. 51, pp. 1835–1844, 2011.

[58] K. Takayama *et al.*, "High-resolution imaging of retinal nerve fiber bundles in glaucoma using adaptive optics scanning laser ophthalmoscopy," *Amer. J. Ophthalmol.*, vol. 155, pp. 870–881, 2013.

[59] J. B. Fisher *et al.*, "Relation of visual function to retinal nerve fiber layer thickness in multiple sclerosis," *Ophthalmology*, vol. 113, pp. 324–332, 2006.

[60] S. Saidha *et al.*, "Primary retinal pathology in multiple sclerosis as detected by optical coherence tomography," *Brain*, vol. 134, pp. 518–533, 2011.

Yuan-Zhi Liu received the B.S. degree in physics and the Ph.D. degree in optics, both from Sun Yat-Sen University, Guangzhou, China, in 2007 and 2012, respectively.

He was a Postdoctoral Researcher with the Ohio State University, Columbus, OH, USA, in 2012. Since 2013, he has been a Postdoctoral Research Associate at the Biophotonics Imaging Laboratory, Beckman Institute for Advanced Science and Technology, University of Illinois at Urbana-Champaign, Urbana, IL, USA. His current research interests include biomedical imaging, especially the development and applications of optical coherence tomography, interferometric synthetic aperture microscopy, hardware/computational adaptive optics, and wavefront shaping.

P. Scott Carney received the B.S. degree in engineering physics from the University of Illinois at Urbana-Champaign, Urbana, IL, USA, in 1994, and the Ph.D. degree from the University of Rochester, Rochester, NY, USA, in 1999.

He was a Postdoctoral Associate with Washington University, St. Louis, MO, USA, from 1999 to 2001. He then joined the Faculty of the Department of Electrical and Computer Engineering, University of Illinois at Urbana-Champaign. His current research interests include inverse problems, imaging, coherence theory, and other branches of optical physics.

Stephen A. Boppart (S'90–M'90–SM'06–F'11) was born in Harvard, IL, USA, in 1968. He received the B.S. degree in electrical and bioengineering and the M.S. degree in electrical engineering from the University of Illinois at Urbana-Champaign, Urbana, IL, in 1990 and 1991, respectively, the Ph.D. degree in electrical and medical engineering from the Massachusetts Institute of Technology, Cambridge, MA, USA, in 1998, and the M.D. degree from Harvard Medical School, Boston, MA, in 2000.

He was a Research Scientist with the Air Force Laser Laboratory, Brooks Air Force Base, San Antonio, TX, USA, where he was involved in research on developing national (ANSI) and air force laser safety standards. Since 2000, he has been at the University of Illinois at Urbana-Champaign, Urbana, from where he completed residency training in internal medicine in 2005. He is currently an Abel Bliss Professor of engineering at the Departments of Electrical and Computer Engineering, Bioengineering, and Medicine, the Head of the Biophotonics Imaging Laboratory, Beckman Institute for Advanced Science and Technology, University of Illinois at Urbana-Champaign, and also the Director of Imaging at Illinois. He has authored or coauthored more than 300 invited and contributed publications, and more than 670 invited and contributed presentations. He holds more than 40 patents, filed or pending. His research interests include the development of novel optical imaging technologies for biological and medical applications, with particular emphasis on translating these to clinical applications.

Dr. Boppart is a Fellow of the IEEE, AAAS, OSA, SPIE, and AIMBE. He is also a Member of the Biomedical Engineering Society, the American Association for Cancer Research, and the American Medical Association. He was named one of the top 100 innovators in the world by the *Technology Review Magazine* for his research in medical technology, and received the IEEE Engineering in Medicine and Biology Society Early Career Achievement Award. He received the Paul F. Forman Engineering Excellence Award from the Optical Society of America for dedication and advancement in undergraduate research education, and recently, the international Hans Sigrist Prize for his work in diagnostic laser medicine.

Fredrick A. South received the B.S. and M.S. degrees in electrical and computer engineering from the University of Illinois at Urbana-Champaign, Urbana, IL, USA, in 2010 and 2013, respectively, where he is currently working toward the Ph.D. degree in electrical and computer engineering.

In 2010, he was an Engineering Intern with Siemens Healthcare, Hoffman Estates, IL, where he focused on electrical engineering of SPECT and PET molecular imaging systems. Since 2011, he has been a Research Assistant at the Biophotonics Imaging Laboratory, Beckman Institute for Advanced Science and Technology, Urbana. His research interests include the development of novel optical imaging modalities for application in medicine and biology.